

Low-Speed Laser Welding of Aluminum Alloy 7075-T6 Using a 300-W, Single-Mode, Ytterbium Fiber Laser

By defining the fluence per weld length and specific weld energy per weld length metrics, the results were examined with respect to power, speed, and focus simultaneously

BY A. G. PALEOCRASSAS AND J. F. TU

ABSTRACT. Heat-treatable aluminum alloys are important structural materials due to their increased strength-to-weight ratio. However, it is challenging to weld heat-treatable aluminum alloys successfully. Some of the factors affecting the weld quality include very high reflectivity, loss of strength, different kinds of porosity formation, hot tearing, solidification cracking, oxide inclusions, loss of alloying elements, and destruction of temper. In this paper, we explored the use of a 300-W, single-mode, ytterbium fiber-optic laser for low-speed keyhole welding of heat-treatable aluminum (7075-T6). The optimum welding speed was found to be between 2 and 3 mm/s, focused slightly into the workpiece (no deeper than 0.75 mm), for a maximum penetration of 1.02 mm. By defining the fluence per weld length and specific weld energy per weld length metrics, we were able to examine the results with respect to power, speed, and focus simultaneously and also get further insight into welding efficiency. The specific weld energy per weld length indicates how “well” the energy was used to produce a high aspect ratio weld. Furthermore, the slope of the plotted curves has a physical meaning as good weld conversion efficiency, indicating how much energy deposited into the material is actually used to produce a “good” weld. Steeper slopes indicate higher weld conversion efficiencies. Results show that with decreasing processing speed, the weld conversion efficiency decreased.

Introduction

Heat-treatable aluminum alloys are important structural materials due to their increased strength-to-weight ratio, com-

A. G. PALEOCRASSAS and J. F. TU (jftu@unity.ncsu.edu) are with the Dept. of Mechanical and Aerospace Engineering, North Carolina State University, Raleigh, N.C.

pared to nonheat-treatable aluminum alloys. However, it is challenging to weld heat-treatable aluminum alloys successfully. Some of the factors affecting the weld quality of aluminum alloys include very high reflectivity, loss of strength, different kinds of porosity formation, hot tearing, solidification cracking, oxide inclusions, loss of alloying elements, and destruction of temper (Refs. 1–3). The particular alloy, AA 7075-T6, though very prone to these weld defects, was chosen for this study because it is one of the most widely used structural materials in aerospace applications.

Laser welding of aluminum has received intensive research interest ever since high-power lasers became relatively affordable. Dausinger et al. reported that with a 2.2-kW Nd:YAG laser, weld depths of up to 3.7 mm in AA 6082 had been obtained at approximately 16.7 mm/s, at a power density of 3 MW/cm² (Ref. 4). Also, Yoshikawa et al. reported that successful butt joint welds of 3-mm-thick Series 6000 aluminum alloys can be obtained (Ref. 5). They also used power modulation (pulsing) to prevent cracks and porosity with a high duty cycle. A 3-kW CO₂ laser has been able to achieve approximately 2.5 mm weld depth in aluminum alloy 7075-T6 at about 25 mm/s (Ref. 6). Also, a 4.5-kW CO₂ produced penetrations of 3.5 mm in aluminum alloy Series 6000, at a speed of approximately 33 mm/s; in comparison, a 4 kW Nd:YAG produced weld depths of 4 mm at the same speed (Ref. 7).

The aforementioned research groups mostly aimed at developing high-speed welding (over 16 mm/s) at relatively high power (over 2 kW) for obvious production advantages and suppression of porosities. However, application areas exist where high speed is not applicable. One of these applications is the fusion of fatigue cracks in aluminum. Due to constant accelerations and decelerations required to follow the irregular crack path, high-speed operation may not be feasible. Furthermore, one of the advantages of welding at lower processing speeds is that the transverse solidification cracking tendency has been shown to decrease due to the reduction of longitudinal strain (Refs. 8, 9).

Fiber Laser Welding

Miyamoto et al. conducted experiments using a single-mode fiber laser for high-speed micro-keyhole laser welding (Ref. 10). In this article, we explored the use of a 300-W, single-mode, ytterbium fiber-optic laser for low-speed keyhole welding of heat-treatable aluminum (7075-T6) for potential applications of crack repair.

The characteristic that sets fiber lasers apart from Nd:YAG lasers is its excellent beam quality, with an M² value of approximately 1.04. This allows the beam to be focused on much smaller spots and, therefore, it is possible to achieve higher power densities. In addition to the excellent beam quality, this laser has a wavelength of approximately 1075 nm (near infrared spectrum), which is relatively short compared to CO₂ lasers. This allows good beam absorption which is needed when welding highly reflective materials like aluminum. The beam diameter exiting the collimator is approximately 4.5 mm, and it can be focused down to approximately 11.5 μm through the use of a 5× beam expander and a 150-mm focal length lens. At 311 W, a max power density of about 300

KEYWORDS

Heat-Treatable Aluminum Alloys
AA 7075-T6
Fluence per Weld Length
Specific Weld Energy per Weld Length
Keyhole Welding

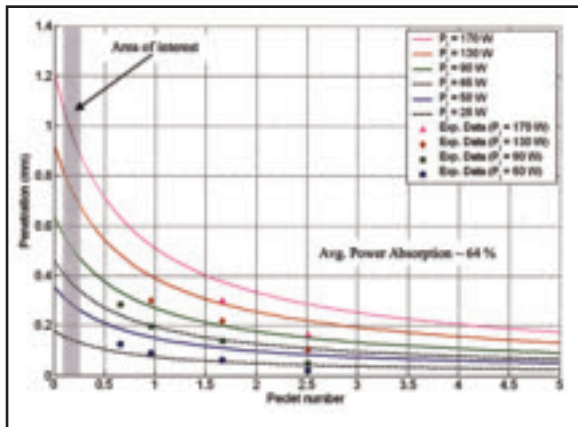


Fig. 1 — Weld penetration comparison of theoretical vs. experimental data (SUS 304) from Miyamoto et al. (Ref. 10).

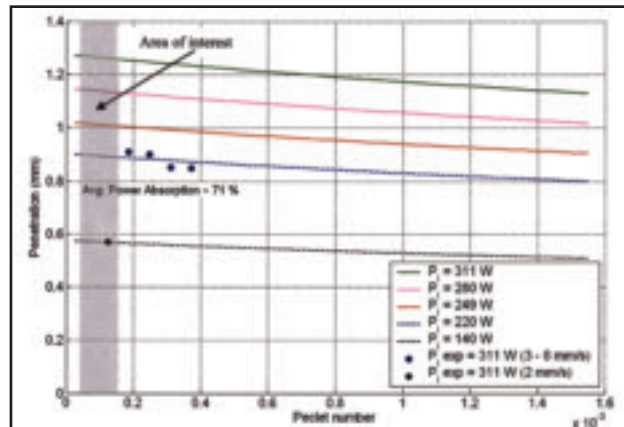


Fig. 2 — Upper bound weld penetration estimation for AA 7075-T6.

MW/cm² can be achieved. Therefore, a fiber laser combines the advantages of CO₂ and Nd:YAG lasers, and it would be interesting to see if it can be used to overcome some of the obstacles associated with laser welding aluminum alloys.

The rest of this paper is organized as follows: A 2D heat conduction model developed by Lankalapalli, Tu, and Gartner was used to predict the upper bound (best case scenario) penetration for a processing speed range between 2 and 6 mm/s (Ref. 11). A technique was developed to determine the beam profile which enabled us to calculate parameters such as power density and fluence per weld length. Next, the experimental results of the bead-on-plate welds for different processing conditions (speed and focus) are presented. A new welding process characterization that takes into account power, processing speed, and beam size is described. A metric is introduced that characterizes the weld size and its aspect ratio corresponding to the fluence deposited into the workpiece. Concluding remarks and future work are presented at the end of the paper.

Welding Penetration Prediction

Before proceeding with experimentation, a theoretical model proposed by Lankalapalli, Tu, and Gartner is used to predict the upper bound behavior of the welding process (Ref. 11). The major assumptions of this model are as follows: a) the keyhole shape is approximated as conical; b) the keyhole is broken down into infinitesimally thin layers and each layer is treated as a 2D cylindrical moving heat source problem; c) the model assumes 100% beam power absorption through the keyhole wall; and d) the heat conduction between layers is negligible. If vapor/plasma effects are not significant, the keyhole can be approximated very well by a conical shape (Ref. 12).

Another assumption is that there is a quasi-steady-state environment in which there is a cylindrical surface of radius a , at uniform temperature T_V , moving with a constant speed, v , along the x direction, in an infinite medium initially at constant temperature, T_0 . Finally, assuming that the thermal properties of the medium are constant and that the axis of the cylindrical surface passes through the origin of the coordinate system, the governing differential equations and boundary conditions for the temperature distribution can be written as follows (Ref. 13):

$$\frac{\partial^2 T}{\partial r^2} + \frac{1}{r^2} \frac{\partial^2 T}{\partial \theta^2} + \left(\frac{1}{r} + \frac{v}{\alpha} \cos \theta \right) \frac{\partial T}{\partial r} - \frac{v}{\alpha} \frac{\sin \theta}{r} \frac{\partial T}{\partial \theta} = 0 \quad (1)$$

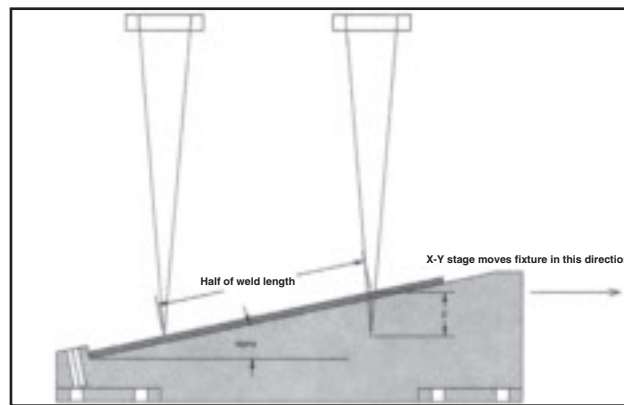


Fig. 3 — Focusing test.

$$T = T_V \text{ at } r = a \quad (2)$$

$$T(r, \theta) \rightarrow T_0 \text{ as } r \rightarrow \infty \quad (3)$$

where r and θ are the surface coordinates, a is the keyhole radius, v is the welding speed, α is the thermal diffusivity, T_0 is the initial temperature, and T_V is the vaporization temperature of the material.

The closed-form solution to Equation 1 is given by the following:

$$\frac{T_V - T}{T_V - T_0} = 1 - e^{-(Pe \cdot r \cdot \cos \theta)} \cdot \sum_{n=0}^{\infty} \epsilon_n \frac{I_n(Pe)}{K_n(Pe)} \cdot K_n(Pe \cdot r^*) \cdot \cos(n \cdot \theta) \quad (4)$$

where $Pe = v \cdot a / (2 \cdot \alpha)$ is the Péclet number, $r^* = r/a$ is the normalized radial coordinate, $\epsilon_n = 1$ for $n = 0$ and 2 for $n \geq 1$, I_n is a modified Bessel function of the first kind, of order n , and K_n is a modified Bessel function of the second kind of order n .

Based on Equations 1-4 and the as-

Table 1 — Assumed Thermal-Physical Properties

	SUS 304 (Stainless Steel)	AA 7075-T6
Thermal Conductivity, k (W/(m ² °K))	21.5	130
Specific Heat Capacity, C_p (J/(kg ² °K))	500	960
Density, ρ (kg/m ³)	8000	2800
Thermal Diffusivity, α (m ² /s)	$5.375 \cdot 10^{-6}$	$48.36 \cdot 10^{-6}$

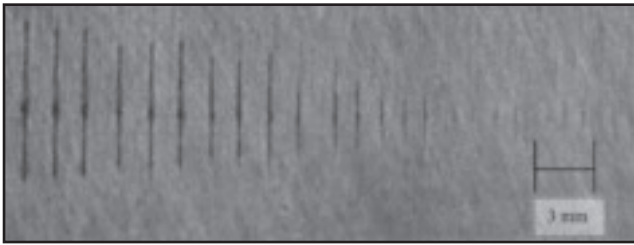


Fig. 4 — Marks created during beam profile test (full view).

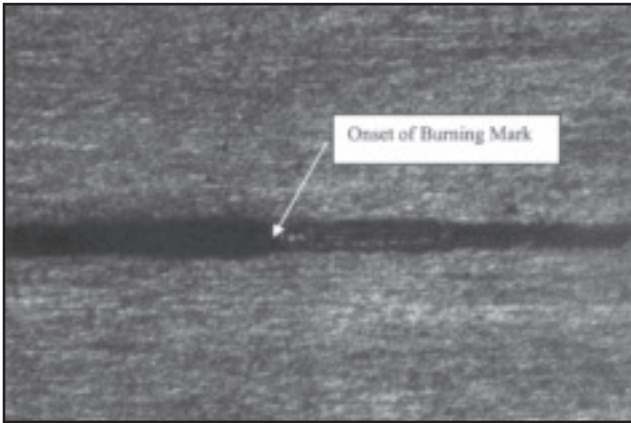


Fig. 5 — Mark created during beam profile test (enlarged view).

assumptions described earlier, the following equation, which estimates weld penetration, was found as (Ref. 11):

$$d = \frac{P_i}{k \cdot (T_V - T_0)} \cdot \frac{1}{\sum_{i=1}^6 \frac{c_i}{i} \cdot (Pe_0)^{i-1}} \quad (5)$$

where Pe_0 is the Péclet number at the surface (calculated with a_0 as the keyhole radius at the surface), k is the thermal conductivity of the material, and c_i are numerically determined coefficients based on Equation 4 with the specified boundary conditions (Equations 2 and 3) for the temperature distribution. This model was validated via bead-on-plate welding of mild steel using a 5-kW CO₂ laser with penetration up to 6 mm (Ref. 11).

In this paper, we provide another validation of the above model using data from Miyamoto et al. in which several SUS 304 specimens, 300 microns thick, were welded as bead-on-plate (partial penetration) at relatively high speeds (200–1000 mm/s) with power levels from 50 to 170 W. This validation justifies the use of this model for the performance upper bound prediction with fiber laser welding. Figure

1 shows the prediction based on the above model as compared to the data. The assumed thermal-physical properties used in this model are listed in Table 1 (SUS 304 stainless steel at high temperature). The data match the model very well in terms of the trend of penetration depth vs. different Péclet numbers. However, it is apparent that the data have lower penetration values than the corresponding theoretical curves, as the data match the curves generated for a lower irradiated laser power (dashed lines). This suggests that some portion of the laser power is not absorbed by the workpiece, which violates the aforementioned assumption (c) that was made for this model. This is reasonable because the model does not account for power losses due to beam reflection, beam scattering, vaporization of material, and beam absorption by vapor/plasma. According to Fig. 1, the average beam absorption by the workpiece is 64% for all cases.

Upper Bound Prediction for Low-Speed Welding of AA 7075-T6: Also indicated in Fig. 1 is the region of interest in this study with a low Péclet number but with higher penetration. We then apply the model for welding of AA 7075-T6 at very low Péclet numbers for three different powers (311, 280, and 249) (Fig. 2). The thermal-physical properties of AA 7075-T6 are listed in Table 1. In Fig. 2, some initial welding results are also plotted and compared to the theoretical prediction. From Fig. 2, a 71% beam absorption ratio is found for welding speeds between 3 and 6 mm/s, while the beam absorption ratio at 2 mm/s is significantly lower at 45%. The difference in the beam

absorption ratio presented in Figs. 1 and 2 is expected because they dealt with different materials and were conducted at very different welding speeds and other process parameters (focusing, assist gas, etc.). However, these absorption ratios are in the same order of magnitude. Due to this significant discrepancy between the data and the simulation for welding at 2 mm/s, it is essential to investigate the parameters critical to the welding process from its upper bound performance at lower speeds. The rest of this paper illustrates a systematic process characterization to correlate the penetration and efficiency to laser power, speed, and focusing.

Beam Profile Test

In this section, an experiment is designed to determine the beam profile; thus, the beam diameter along its propagation direction. This information is needed because it allows us to calculate the laser power density at the workpiece surface for different focusing positions. Although dedicated instruments can be used for this purpose, the proposed method is simple, practical, and inexpensive.

As shown in Fig. 3, the laser beam is irradiated along an angled plate. It is assumed that during the test, at a specific laser power and traveling speed, a burn mark starts to form when the fluence per weld length reaches a threshold. This threshold is expressed as

$$f_c = \frac{P}{\pi \cdot r_i^2} \cdot \frac{l_i}{v_i} / l_i = \frac{P}{\pi \cdot r_i^2 \cdot v_i} \quad (6)$$

$i = 1, 2, \dots, n$

where f_c is the critical fluence per weld length in J/cm³, P is the incident power in watts, r_i is the beam radius at the onset of the burn mark in centimeters, l_i is the total length of the burning mark, and v_i is the processing speed. The value of f_c indicates the

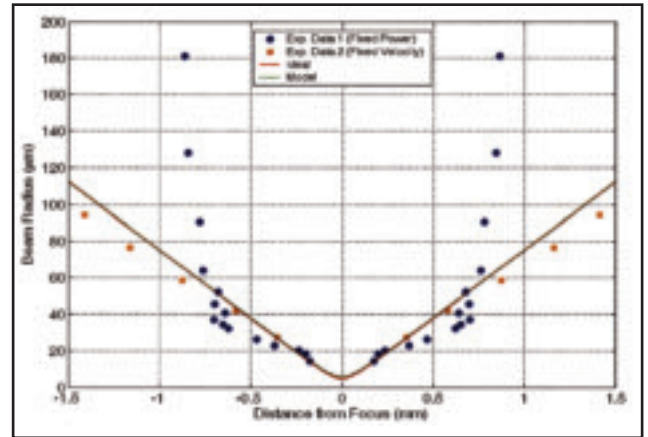


Fig. 6 — Spot radius as a function of focusing depth (150-mm lens).

amount of energy per area for a unit length of weld that is required in order to form a weld in AA 7075-T6. This value is assumed to be constant for a specific material.

Based on Equation 6, we can either keep the power constant and change the processing speed or keep the speed constant and change the power to generate different burning marks. If the power is kept constant, the spot radius at the onset of the burning mark can be determined as

$$r_i = \sqrt{\frac{P}{\pi \cdot v_i \cdot f_c}} \quad (7)$$

Similarly, Equation 7 can be modified easily if the speed is kept constant. For the analysis of near field beam profile, it is preferred to keep the power constant instead of speed of more accurate control (fewer fluctuations). Equation 7 provides information about the critical spot radius at the onset of the burning mark. The vertical position of the critical spot radius can be determined from geometry as

$$z = \frac{l_w}{2} \cdot \sin \alpha \quad (8)$$

where α is the angle of the tilted workpiece, l_w is the length of the mark, and z is the distance from the focal point of the laser. By conducting several burning tests at a fixed speed and a fixed power, Equations 7 and 8 are used to provide the beam profile along the beam propagation direction, based on the length of the burning marks (l_w).

Figures 4 and 5 show the results of these beam profile tests at a constant power where Fig. 4 shows an array of tests, and Fig. 5 shows a portion of one pass. In Fig. 4, the speed increases from 0.0625 to 2.0 mm/s going toward the right, causing the marks to become shorter. These tests were done in groups of three, so each group of three is a single speed with the next group of three at a faster speed. The point at which a consistent melting action is observed is considered to be the point where measurement is performed.

To use Equations 7 and 8, the value of f_c must be determined. The classical beam propagation model (Ref. 14) is

$$r(z) = r_0 \cdot \sqrt{1 + \left(\frac{M_0^2 \cdot \lambda \cdot z}{\pi \cdot r_0^2} \right)^2} \quad (9)$$

where $r(z)$ is the radius at position z , r_0 is the minimum radius, M_0^2 is the beam qual-

ity index, and λ is the beam wavelength. The relationship between minimum spot size, far-field divergence angle (θ), and beam quality is

$$r_0 \cdot \theta = \frac{M_0^2 \cdot \lambda}{\pi} \quad (10)$$

For a focusing lens with a focal length f and beam radius at the lens R_0 , θ can be approximated as R_0/f and the minimum spot size can be written as

$$r_0 = \frac{M_0^2 \cdot \lambda \cdot f}{\pi \cdot R_0} \quad (11)$$

Due to optical errors, Equation 9 needs to be modified based on Essien and Fuerschbach (1996) to replace M_0^2 as

$$M^2 = M_0^2 + \frac{a}{f^2} \quad (12)$$

where a is a constant related to f_c via Equations 7 and 11 and needs to be determined experimentally (Ref. 15).

The value of constant a is determined through an iteration process. First, a value for constant a is assumed in Equation 12 and then the minimum spot size is determined using Equation 11. This spot size is then used in Equation 9 and in turn $r(z)$ is used in Equation 7 to determine f_c . With the value of f_c determined, Equations 7 and 8 along with Figs. 4 and 5 are used to plot the beam profile compared with the theoretical profile determined by Equations 9 and 12. Then this process is iterated until a proper fit is achieved. The resulting beam profile is shown in Fig. 6.

Figure 6 shows the data plotted versus the plot of the ideal and modified beam propagation equations. For the data set with a constant power, the near-field data ($-0.25 \leq z \leq 0.25$ mm) are in good agreement with the theoretical model while the far-field data deviate from the model substantially. For the data set with a constant speed, the far-field data show better agreement with the theoretical model. Note that the near-field data below 0.35 mm at constant speed are not achievable due to the low power limit of the laser.

The reason for the deviation in the far-field region for the data set at a constant power is likely due to the inconsistency in the determination of the onset point. In the tests to determine the far-field data, the travelling speed was reduced to 0.25, 0.125, and 0.0625 mm/s. At these lower speeds, the beam absorption mechanism might have changed, causing inconsis-

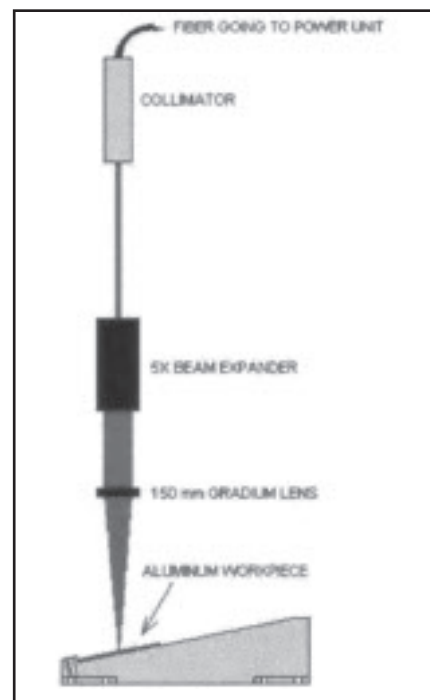


Fig. 7 — Experimental setup.

tency in the onset point. This observation is supported by the better agreement at far-field by the data set with a constant speed at 0.5 mm/s with power from 15 to 40% of the total laser power.

The minimum spot diameter is determined from Fig. 6 as 11.5 μm for a 150-mm lens, as compared with the ideal diameter of 9.49 μm . Correspondingly, the M^2 value changed from 1.04 to 1.26, a 21.2% increase. For comparison, the results of Essien and Fuerschbach showed that for a similar focal length lens of 190 mm, with respect to the 10.6- μm beam, the M^2 value went from 1.5 to 1.9, a 26.7% increase (Ref. 15). The beam profile in Essien and Fuerschbach was determined using a scanning probe. This increase in the M^2 value of our laser beam is mainly due to the spherical aberration from optical elements in the beam expander. Separate tests using only the gradium focusing lens without the beam expander show little or no increase in the M^2 value.

Bead-On-Plate Welding Experiments

In order to determine the general behavior of welding AA 7075-T6, partial penetration bead-on-plate tests were conducted. This helped reduce complexity by decreasing the number of parameters that affect the outcome of the process.

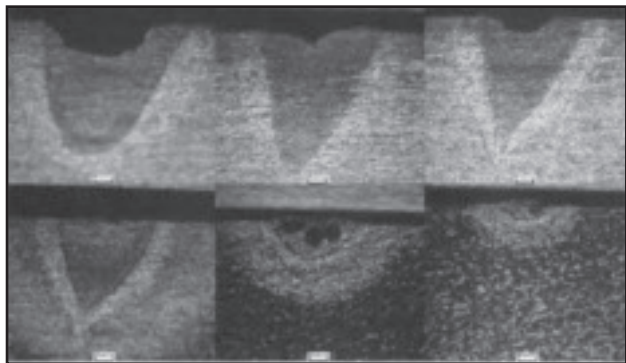


Fig. 8 — Weld cross sections for 6 mm/s at 311 W (with 100-µm delimiters).

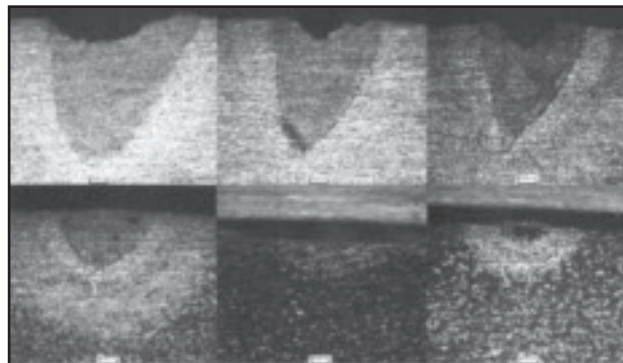


Fig. 9 — Weld cross sections for 5 mm/s at 311 W (with 100-µm delimiters).

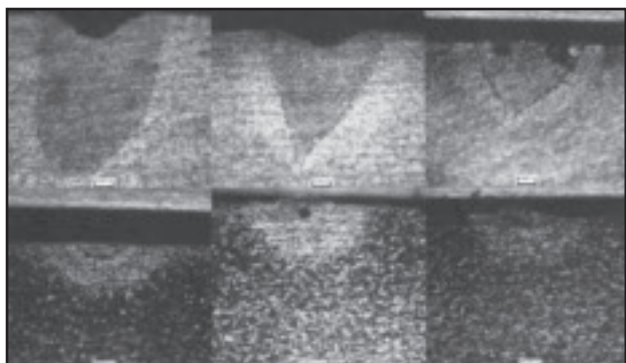


Fig. 10 — Weld cross sections for 4 mm/s at 311 W (with 100-µm delimiters).

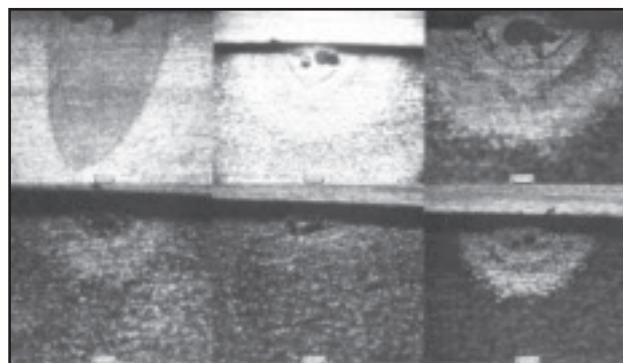


Fig. 11 — Weld cross sections for 3 mm/s at 311 W (with 100-µm delimiters).

The laser and specimen were set up in a way shown in Fig. 7. Due to the high reflectivity of aluminum, it is necessary that the workpiece is tilted at an angle; otherwise, the beam reflected back up through the optics may damage the collimator and the laser. The remaining experiments were also conducted using fixtures that would tilt the workpiece at an angle of approximately 12 deg.

The beam exits the collimator at a diameter of approximately 4.5 mm and is expanded 5 times using the beam expander. After it exits the beam expander it is focused down to the desired spot size (approximately 11.5 µm in diameter). Shielding gas (helium) is used to prevent any oxidation from occurring in addition to blowing away most of the generated plasma.

Figure 8 shows the cross sections for the welding speed of 6 mm/s at 311-W power. From left to right, the top row shows the welds resulting from focusing depth of 0 (surface of the workpiece), 0.75, and 1 mm. The bottom row (from left to right) shows the resulting cross sections from focusing depth of 1.25, 1.5, and 1.75 mm. It is rather obvious that the deepest penetration occurs at focusing depths of 0.75 and 1 mm. Also, it is apparent that when the beam is focused too deep, the

weld hardly has any penetration and resembles the conduction welding mode rather than the keyhole mode. At 1.25-mm focusing depth, a nice weld starts to form and increases in penetration at 1-mm focusing depth. Instead of increasing in penetration, the weld just becomes wider. At the surface welding condition the weld seems to be wider and shallower, probably due to more plasma generation. Since the focusing is so critical with the incline, it is also possible that the beam was focused slightly above the surface, which would mean that the beam would start diverging into the workpiece.

Another factor that needs to be considered is the weld quality. From a quick glance it seems that the deeper welds (focusing depth between 0 and 1.25 mm) are free from major defects. One of the defects present that is of concern is the underfill that occurs at the surface. This is probably due to the weld spatter that occurs as well as vaporization of alloying elements. The other two weld cross sections seem to have either some type of porosity or inclusion in the weld. This can occur in a number of different ways — from shielding gas or hydrogen (moisture in the air) getting entrapped and not having enough time to escape before the molten pool so-

lidifies, to aluminum oxides getting mixed in the molten pool.

Figure 9 shows the cross sections for 5 mm/s speed, at 100% power, for the same focusing depths (in the same order).

In this case, the trend is pretty similar with the exception that the deepest penetration is achieved at the surface weld. Again, as the focusing moves closer and closer to the surface, the rate at which penetration increases drops dramatically. Instead, the weld increases in width and only slightly in penetration.

For the higher power density welds, again, underfill can be observed. However, no major porosities or inclusions seem to be present.

In Fig. 10, the same trend seems to be going on. For the focusing depths of 1.25 through 1.75, there is little to no penetration. At 1 mm a weld starts to form, and at 0.75 mm the penetration increases significantly. Finally, for the surface weld, the penetration increases slightly, but the weld width increases noticeably.

Consistently, the deeper welds seem to be free of major porosities and inclusions but have an underfill “dimple.” In the rest of the welds some porosity can be detected.

Figure 11 shows the cross sections re-

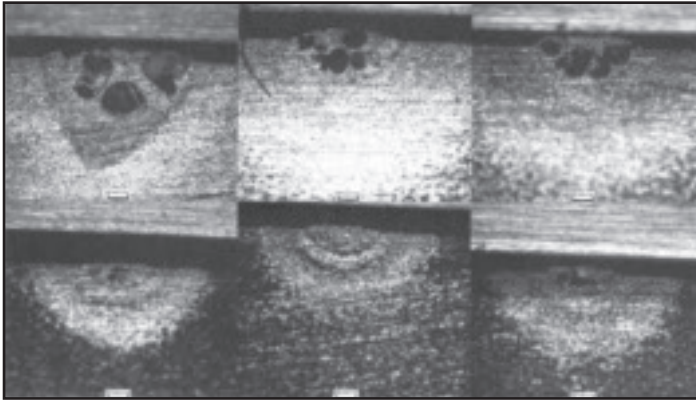


Fig. 12 — Weld cross sections for 2 mm/s at 311 W (with 100- μ m delimiters).

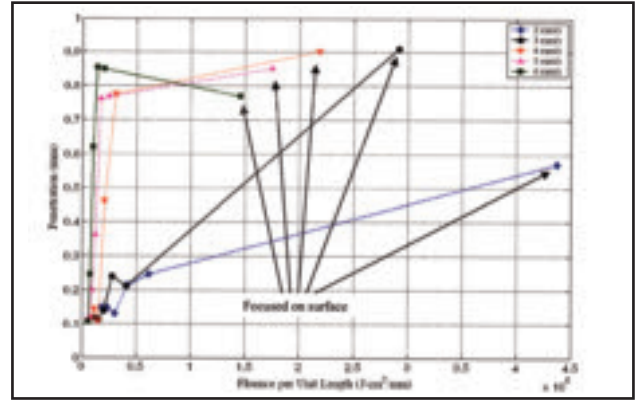


Fig. 13 — Penetration values at different speeds (311 W).

sulting from a welding speed of 3 mm/s at 311 W.

This welding condition yields the highest penetration so far, but the rest of the welds are very bad. They have little to no penetration, and they are full of cavities. Again, the deep penetration weld is practically defect free, with the exception of the small underfill.

Finally, in Fig. 12, the cross sections are shown of welding at a speed of 2 mm/s at 311 W. These were by far the most unsuccessful welds that were run at 311 W. They achieved barely any penetration, and the ones that did had a significant amount of defects in them.

Welding Process Characterization

To characterize all the welding results of Figs. 8–12 in one chart for more insightful information, we define a new parameter, fluence per weld length (\hat{F}), to relate the focusing position and the welding speed:

$$\hat{F} = \frac{P}{\pi \cdot r^2} \cdot \frac{l_{\text{weld}}}{v} / l_{\text{weld}} = \frac{P}{\pi \cdot r^2 \cdot v} \quad (13)$$

where P is total power output, r is the spot radius as calculated from the beam profile (Fig. 6), l_w is the total weld length, and l_w/v is the total welding time. The value of \hat{F} indicates how much energy is deposited per area for a unit length of weld from the laser. Based on the results of Figs. 8–12, we can plot a chart of penetration depth (d) versus fluence per weld length (\hat{F}) for all five welding conditions at 311 W — Fig. 13.

Five curves are plotted in Fig. 13, corresponding to welds at five different welding speeds from 6 to 2 mm/s. We first investigate the 6 mm/s line, which is the first

one from the left. As indicated by this line, penetration depth increases almost linearly as \hat{F} increases, corresponding to focusing moving from 1.75 to 1.0 mm into the material. A similar characterization using penetration depth versus power density was reported by Dausinger et al. (Ref. 4). With the definition of \hat{F} , we are able to include the welding speed in the process characterization. This linear trend breaks down as the focus moves further up to be less than 1.0 mm into the material. Instead, the penetration depth levels off and even decreases. Examining the weld shapes for conditions on the steep slope, in particular at 1.25 and 1.0 mm, we find that their weld shapes are consistent with weld shapes resulting from a conical keyhole as predicted by the model developed by Lankalapalli, Tu, and Gartner (Ref. 11). A conical keyhole shape indicates that the beam absorption is mostly due to the Fresnel absorption as described in Tu et al. (Ref. 12). This is additional evidence to support that the conical keyhole condition is an ideal welding condition as discussed in the section titled welding penetration prediction. At focus position of 0.75 and 0 mm into the material, even though \hat{F} is higher, it does not result in deeper penetration and large underfill develops.

Interestingly, the three lines corresponding to 6, 5, and 4 mm/s demonstrate almost identical linear slopes, indicating identical keyhole beam absorption mechanism. At 3 and 2 mm/s, the d versus \hat{F} slope is not as steep as in higher speeds, indicating a less ideal welding condition even though higher \hat{F} is deposited to the material surface.

In summary, based on the process characterization of Fig. 13, it is an advantage to be able to design a welding process residing on a steep slope for most efficient conversion of laser energy to penetration depth. However, an upper bound in penetration depth is soon reached as predicted

in Fig. 2. On the other hand, even though poor welding conditions reside in the region of high \hat{F} (which corresponds to low speed and therefore low Péclet number), this region provides a higher upper bound in penetration depth and is the region of great interest in this study (see Fig. 2). It will be beneficial to improve the welding condition in this region so that much deeper penetration can be achieved. This will be addressed in the next section. The maximum penetration achieved for these settings was just over 0.9 mm.

Welding Efficiency

To investigate the major shift in the beam absorption mechanism in the high \hat{F} area, we developed another metric based on the total energy used to produce a weld, denoted as specific weld energy per weld length (\hat{E}) and compare it to total fluence per weld length (\hat{F}) deposited. The value of \hat{E} is determined as

$$\begin{aligned} \hat{E} &= m_{\text{weld}} \cdot \zeta / (\pi \cdot r_{\text{profile}}^2) l_{\text{weld}} \\ &= \rho \cdot V_{\text{weld}} \cdot \zeta / (\pi \cdot r_{\text{profile}}^2) l_{\text{weld}} \\ &= \rho \cdot A_{\text{weld}} \cdot l_{\text{weld}} \cdot \zeta / (\pi \cdot r_{\text{profile}}^2) l_{\text{weld}} \\ &= \rho \cdot A_{\text{weld}} \cdot \zeta / (\pi \cdot r_{\text{profile}}^2) \end{aligned} \quad (14)$$

where m_{weld} , V_{weld} , A_{weld} , and l_{weld} are the mass, volume, cross-sectional area, and length of the weld, respectively, r_{profile} is half the weld's cross-sectional width at the top of the weld, ρ is the density, and ζ is the specific energy of the material and is determined by Equation 15.

$$\zeta = C_p \cdot \Delta T + \Delta E \quad (15)$$

where C_p is the specific heat, ΔT is the temperature rise from room temperature to melting temperature, and ΔE is the la-

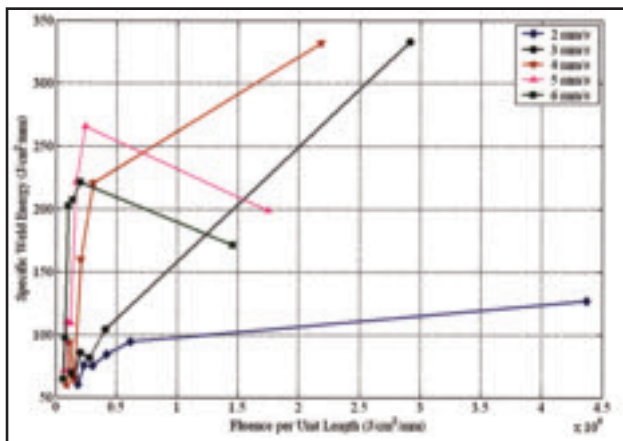


Fig. 14 — Variation of weld energy per unit length with increase in fluence per unit length (311 W).

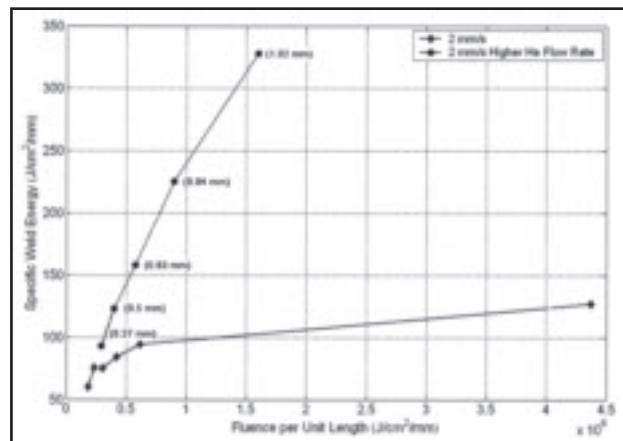


Fig. 15 — Comparison between 2 mm/s welds with different helium flow rates (311 W).

tent heat of fusion of AA 7075-T6.

According to Equation 14, the value of \hat{E} can be determined from the cross-sectional area of the weld based on the weld images — Figs. 8–12. We can now plot the relationship between \hat{E} and \hat{F} as shown in Fig. 14 for 311 W.

At first, it might not be very intuitive why \hat{E} is an important quantity. \hat{E} represents the total energy per unit length used to form the weld, divided by the area calculated using half of the weld width as the radius. This quantity tells us how “well” the energy is used to produce a quality weld. For example, two welds that have the same cross-sectional area but different weld widths are not necessarily equally desirable. The weld with the smaller width (higher aspect ratio) is going to have deeper penetration and therefore a higher \hat{E} .

The slope in Fig. 14 now has a very clearly defined physical meaning as effective weld conversion efficiency, indicating how much energy deposited into the material is actually used to produce a “good” weld. Steeper slopes indicate higher weld conversion efficiency. With the exception of the welds at 2 and 3 mm/s, the welding efficiency (slope of weld energy and fluence) is the same for each welding condition until the fluence per unit length exceeds 0.3 J/cm²/mm. Beyond this value the overall conversion efficiency drops significantly. Also, as fluence increases, the efficiency drops, but again is approximately the same with speeds of 4, 5, and 6 mm/s. Another observation that has been made is that with slower speeds, higher fluence per length is possible, but the specific weld energy increases only slightly and the efficiency drops dramatically, especially at a welding speed of 2 mm/s.

One would expect that with slower speeds, the energy absorbed would be

higher due to the higher fluence. However, the increase in absorbed energy is not as expected. In fact, it only increases slightly and then drops back down. Based on the weld images of Fig. 12, it is indicated that the weld shape is no longer consistent with those resulting from a conical keyhole, indicating the Inverse Bremsstrahlung (IB) absorption might have become significant due to high concentration of the plasma inside the keyhole (Ref. 12). Keyhole plasma absorbs and redirects a portion of laser energy, keeping it from reaching deeper into the material. A common practice that is a partial solution to this problem is to use a higher shielding gas flow rate to blow away the plasma.

In order to verify the assumption that the plasma plume is a contributing factor to the lower welding efficiency at a welding speed of 2 mm/s, the experiment was repeated for those conditions with a higher shielding gas flow rate (from 28 to 32 L/min). The results are compared to the original results at the same welding speed in Fig. 15. Our preliminary results show that an increase in the flow rate increases the weld efficiency. Further research is needed to establish the mechanism that affects penetration at low speeds.

With the exception of the weld that had the beam focused on the surface, the rest of the welds were without any underfill. However, they did have some inclusions and porosities. The deepest weld was achieved at a focusing depth of 0.75. The penetration depth was 1.02 mm.

Summary and Future Work

The 300-W Ytterbium, single-mode fiber-optic laser has been used to create bead-on-plate welds. The optimum weld-

ing speed is between 2 and 3 mm/s, focused slightly into the workpiece (no deeper than 0.75 mm), for a maximum penetration of 1.02 mm — Fig. 15. This is compared with the upper bound prediction of approximately 1.25-mm penetration using the model developed by Lankalapalli, Tu, and Gartner (Ref. 11).

By defining the fluence per weld length and specific weld energy per weld length metrics, we were able to examine the results with respect to power, speed, and focus simultaneously and also get further insight in welding efficiency. The specific weld energy per weld length indicates how “well” the energy was used to produce a high aspect ratio weld. Furthermore, the slope of the plotted curves has a physical meaning as effective weld conversion efficiency, indicating how much energy deposited into the material is actually used to produce a “good” weld. Steeper slopes indicate higher weld conversion efficiency. Results show that with decreasing processing speed, the weld conversion efficiency decreased. In other words, the melting efficiency decreased with processing speed. The energy that was not directly used to generate welds is either carried away as heat conduction loss, reflected away by the workpiece, or loss due to scattering and absorption vapor/plasma.

Finally, a cost-effective method was also developed to approximate the beam profile at and around the focused spot. This can prove to be a useful tool to approximate the power density distribution at different focusing depths.

This investigation has shown that there is great potential for welding heat-treatable aluminum alloys with fiber optic lasers. The biggest obstacle so far has been aluminum alloys’ high reflectivity. If the workpiece is positioned perpendicular to

the beam, it reflects some of it back into the collimator and damages it. One of the solutions to this problem is to fit an optical isolator onto the collimator, which will divert the reflected beam away from it. Although the beam quality may be sacrificed slightly, some of the problems that occur with the current (tilted) setup will be eliminated. Currently, any variation perpendicular to the weld direction will change the focus of the beam with respect to the workpiece. Other areas in which research needs to be pursued in the future include vapor/plasma effects, shielding gas flow rate control, different joint configuration (leading up to crack repair), microstructure examination, and defect suppression.

Acknowledgments

This work has been supported in part by NSF Grants #DMI 0355481 and #DMI 0355214, as well as state funding from the Department of Mechanical and Aerospace Engineering, North Carolina State University.

References

1. Duley, W. W. 1999. *Laser Welding*. John Wiley & Sons, Inc., pp. 114–136.
2. Dawes, C. 1992. *Laser Welding*. McGraw-Hill, Inc., pp. 51–150.
3. Ramasamy, S., and Albright, C. E. 2000. CO₂ and Nd:YAG laser beam welding of 6111-T4 aluminum alloy for automotive applications. *Journal of Laser Applications* 12(3): 101–115.
4. Dausinger, F., Rapp, J., Beck, M., Faisst, Hack, R., and Hugel, H. 1996. Welding of aluminum: a challenging opportunity for laser technology. *Journal of Laser Applications* 8(6): 285–290.
5. Yoshikawa, M., Kurosawa, T., Nakata, K., Kimura, S., and Aoki, S. 1995. YAG laser welding of aluminum alloys. *Journal of Light Metal Welding & Construction* 32(9): 15–23.
6. Katayama, S., and Mizutani, M. 2002. Laser weldability of aluminum alloys. *Trans. JWRI* 31(2): 147–155.
7. Cao, X., Wallace, W., Immarigeon, J.-P., and Poon, C. 2003. Research in laser welding of wrought aluminum alloys. I. Laser welding processes. *Materials and Manufacturing Processes* 18(1): 1–22.
8. Hu, B., and Richardson, I. M. 2006. Mechanism and possible solution for transverse solidification cracking in laser welding of high strength aluminum alloys. *Materials Science and Engineering A* 429(1–2): pp. 287–294.
9. Hu, B., and Richardson, I. M. 2006. Hybrid laser/GMA welding aluminium alloy 7075. *Welding in the World* 50(7–8): pp. 51–57.
10. Miyamoto, I., Park, S.-J., and Ooie, T. 2003. Ultrafine-keyhole welding process using single-mode fiber laser. *Proc. of ICALAO*, 203–212.
11. Lankalapalli, K. N., Tu, J. F., and Gartner, M. 1996. A model for estimating penetration depth of laser welding processes. *Journal of Phys. D, Appl. Phys.* 29(7): 1831–1841.
12. Tu, J. F., Inoue, T., and Miyamoto, I. 2003. Quantitative characterization of keyhole absorption mechanisms in 20 kW-class CO₂ laser welding processes. *Journal of Phys. D, Appl. Phys.* 29(2): 192–203.
13. Carslaw, H. S., and Jaeger, J. C. 1962. *Conduction of Heat in Solids*, 2nd ed. Oxford: Clarendon, p. 390.
14. Steen, W. M. 2003. *Laser Material Processing*, 3rd ed. Springer-Verlag London Limited, pp. 84–90.
15. Essien, M., and Fuerschbach, P. W. 1996. Beam characterization of a materials processing CO₂ laser. *Welding Journal* 75(2): 47s to 54s.

Preparation of Manuscripts for Submission to the *Welding Journal* Research Supplement

All authors should address themselves to the following questions when writing papers for submission to the *Welding Research Supplement*:

- ◆ Why was the work done?
- ◆ What was done?
- ◆ What was found?
- ◆ What is the significance of your results?
- ◆ What are your most important conclusions?

With those questions in mind, most authors can logically organize their material along the following lines, using suitable headings and subheadings to divide the paper.

1) **Abstract.** A concise summary of the major elements of the presentation, not exceeding 200 words, to help the reader decide if the information is for him or her.

2) **Introduction.** A short statement giving relevant background, purpose, and scope to help orient the reader. Do not duplicate the abstract.

3) **Experimental Procedure, Materials, Equipment.**

4) **Results, Discussion.** The facts or data obtained and their evaluation.

5) **Conclusion.** An evaluation and interpretation of your results. Most often, this is what the readers

remember.

6) **Acknowledgment, References and Appendix.**

Keep in mind that proper use of terms, abbreviations, and symbols are important considerations in processing a manuscript for publication. For welding terminology, the *Welding Journal* adheres to AWS A3.0:2001, *Standard Welding Terms and Definitions*.

Papers submitted for consideration in the *Welding Research Supplement* are required to undergo Peer Review before acceptance for publication. Submit an original and one copy (double-spaced, with 1-in. margins on 8 ½ x 11-in. or A4 paper) of the manuscript. A manuscript submission form should accompany the manuscript.

Tables and figures should be separate from the manuscript copy and only high-quality figures will be published. Figures should be original line art or glossy photos. Special instructions are required if figures are submitted by electronic means. To receive complete instructions and the manuscript submission form, please contact the Peer Review Coordinator, Erin Adams, at (305) 443-9353, ext. 275; FAX 305-443-7404; or write to the American Welding Society, 550 NW LeJeune Rd., Miami, FL 33126.